Two-dimensional quantum universality in the spin-1/2 triangular-lattice quantum antiferromagnet $Na_2BaCo(PO_4)_2$

Jieming Sheng[a,b,c,d,1] [iD], Le Wang[a,e,1], Andrea Candini[f] [iD], Wenrui Jiang[a,e], Lianglong Huang[a,e], Bin Xi[g], Jize Zhao[h], Han Ge[a] [iD], Nan Zhao[a] [iD], Ying Fu[a,e], Jun Ren[a], Jiong Yang[i], Ping Miao[c,d], Xin Tong[c,d], Dapeng Yu[e,a], Shanmin Wang[a], Qihang Liu[a] [iD], Maiko Kofu[j], Richard Mole[k], Giorgio Biasiol[l], Dehong Yu[k,2], Igor A. Zaliznyak[m,2] [iD], Jia-Wei Mei[a,e,n,2], and Liusuo Wu[a,n,2] [iD]

An interplay of geometrical frustration and strong quantum fluctuations in a spin-1/2 triangular-lattice antiferromagnet (TAF) can lead to exotic quantum states. Here, we report the neutron-scattering, magnetization, specific heat, and magnetocaloric studies of the recently discovered spin-1/2 TAF $Na_2BaCo(PO_4)_2$, which can be described by a spin-1/2 easy axis XXZ model. The zero-field neutron diffraction experiment reveals an incommensurate antiferromagnetic ground state with a significantly reduced ordered moment of about 0.54(2) μ_B/Co. Different magnetic phase diagrams with magnetic fields in the ab plane and along the easy c-axis were extracted based on the magnetic susceptibility, specific heat, and elastic neutron-scattering results. In addition, two-dimensional (2D) spin dispersion in the triangular plane was observed in the high-field polarized state, and microscopic exchange parameters of the spin Hamiltonian have been determined through the linear spin wave theory. Consistently, quantum critical behaviors with the universality class of $d = 2$ and $\nu z = 1$ were established in the vicinity of the saturation field, where a Bose–Einstein condensation (BEC) of diluted magnons occurs. The newly discovered quantum criticality and fractional magnetization phase in this ideal spin-1/2 TAF present exciting opportunities for exploring exotic quantum phenomena.

quantum criticality | quantum magnet | neutron scattering | spin frustration | universal scaling

Quantum antiferromagnet with frustrated spin lattices offers an exemplary system for exploring the quantum phase transitions of interacting bosons (1). Starting from the fully polarized state at high magnetic fields, the $S = 1/2$ spins can be exactly mapped onto hard-core bosons. The applied magnetic field which acts as the chemical potential tunes the density of the bosons from zero as lowering field, creating a quantum critical point (QCP) of the Bose–Einstain condensation (BEC) type universality class (2–10). With further lowering field, more bosons are introduced to the frustrated spin lattice, and the interactions between the bosons are no longer negligible. When the frustration is strong and the potential energy is dominating, Wigner crystallization into superlattices with sharp step-like fractional magnetization plateaus is expected (11–13). With special cases, continuous transitions of a supersolid-like coexistence phase may exist as well (14, 15). On the two-dimensional (2D) triangular lattice of spin-1/2, the geometrical frustration leads to a narrow bandwidth for the bosons, and many of these emerged exotic quantum states have been theoretically proposed, depending on the relative strength of the competing interactions (16, 17). Experimentally, for a two-dimensional spin-1/2 triangular-lattice antiferromagnet (TAF), the 1/3 magnetization plateau corresponding to a quantum up–up–down (UUD) state has been observed in several materials, including isosceles triangular lattice system Cs_2CuBr_4 (18–21), the equilateral triangular lattice materials $Ba_3CoSb_2O_9$ (22–25), and the $AYbCh_2$ (A = Na and Cs, Ch = O, S, Se) family (26–29).

Furthermore, field-induced phase transitions in the quantum antiferromagnets provide a unique approach to understanding quantum criticality for the bosonic system. The fermionic system in the heavy-fermion compounds exhibits the quantum universal scaling of thermodynamic properties (30, 31). In a few one-dimensional (1D) bosonic systems, the quantum universal scaling is established (32, 33) in which the transmutation between the fermionic and bosonic statistics occurs (34). Due to the large critical fields that are usually beyond the limit of most laboratory magnets, experimental investigations of the related quantum criticality in the 2D antiferromagnets, e.g., the spin-1/2 triangular-lattices (18, 22, 23), have been rarely explored before. Therefore, it is of great interest to study the quantum universal scaling of thermodynamic properties in the two-dimensional frustrated quantum antiferromagnetic (AFM) compounds that can be easily tuned with external field.

Significance

Although considerable progress has been made in the theoretical understanding of the low-dimensional frustrated quantum magnets, experimental realizations of a well-established scaling analysis are still scarce. This is particularly true for the two-dimensional antiferromagnetic triangular lattices. Owing to the small exchange strength, the newly discovered compound $Na_2BaCo(PO_4)_2$ provides a rare opportunity for clarifying the quantum criticality in an ideal triangular lattice with quantum spin $S = 1/2$. In addition to the establishment of the complete phase diagrams, the spin Hamiltonian with a negligible interplane interaction has been determined through the spin wave dispersion in the polarized state, which is consistent with the observation of a two-dimensional quantum critical point with the Bose–Einstein condensation of diluted free bosons.

[1] J.S. and L.W. contributed equally to this work.

[2] To whom correspondence may be addressed. Email: Dehong.Yu@ansto.gov.au, zaliznyak@bnl.gov, meijw@sustech.edu.cn, or wuls@sustech.edu.cn.

In this work, we investigate the quantum criticality in the 2D bosonic system by studying the field-induced phase transitions in the recently discovered spin-1/2 triangular-lattice antiferromagnet $Na_2BaCo(PO_4)_2$ (35, 36). Measurements of magnetization, specific heat, magnetocaloric effect (MCE) and single crystal neutron scattering have been performed. An AFM phase transition around 0.15 K was observed, with an incommensurate magnetic wave vector located around $(1/3, 1/3, \pm0.167(3))$ in zero field. With applying the in-plane and c-axis directional magnetic fields, different magnetic phase diagrams were explored, which are in overall agreement with the previous theoretical studies (16, 17, 37). The spin-1/2 XXZ model in Eq. **1** on the triangular lattice with parameters derived from the magnetization measurements was further confirmed by the magnon dispersion observed in the fully polarized ferromagnetic state, and a 2D quantum universal scaling was observed.

Results and Discussion

Crystal Strucutre, Effective Spin and Anisotropic Magnetic Interaction.

As shown in Fig. 1*A*, $Na_2BaCo(PO_4)_2$ crystallizes in the trigonal crystal structure ($P\bar{3}m1$) with lattice parameters $a = b = 5.3185$ Å and $c = 7.0081$ Å (35). The magnetic Co^{2+} ions are coordinated to six oxygen atoms (three above and three below the layer), which result in a slightly distorted CoO_6 octahedra without the fourfold symmetry, or it can be viewed as a distorted triangular prism of local D_{3d} ($\bar{3}m$) symmetry. In the crystal ab plane, these Co^{2+} ions form a perfect triangular network, with the layered AA-stacking along the c-axis (Fig. 1 *A* and *B*). The Co^{2+} in this triangular prism crystal field results in

an effective $S = 1/2$ degree of freedom at low energy due to the spin–orbit coupling (38).

The isothermal magnetization, $M(B)$, measured at 2 K for the magnetic field applied along a, a^*, and c directions is shown in Fig. 1*C* (details of the orientation are shown in *SI Appendix*, Fig. S1). For field in the ab plane, the magnetization is nearly isotropic, with the saturation moment $\approx 2.2\,\mu_B/Co$. For field along the c-axis, which is also the local high symmetric direction of the CoO_6 triangular prism, the magnetization is slightly larger, with the saturation moment $\approx 2.5\,\mu_B/Co$ at 6 T. The temperature-dependent DC magnetic susceptibility, $\chi(T)$, with $B \parallel a^*$ and $B \parallel c$ is shown in Fig. 1*D*. The Curie–Weiss law was applied to fit the inverse susceptibility $1/\chi(T)$ from 5 K to 50 K by including a temperature-independent Van Vleck contribution χ_0, as shown by the red solid line in Fig. 1*D*. By the fits, we can obtain the Curie–Weiss temperature $\theta_{CW}^{ab} = -1.51(2)$ K, $\theta_{CW}^c = -2.59(1)$ K and the effective moment $\mu_{eff}^{ab} = 3.61(1)\mu_B/Co$, $\mu_{eff}^c = 4.15(1)\mu_B/Co$ for $B \parallel ab$ and $B \parallel c$, respectively.

We can write down the triangular-lattice spin-1/2 XXZ spin Hamiltonian to model the spin system in $Na_2BaCo(PO_4)_2$

$$H = \sum_{\langle ij \rangle} [J_{xy}(S_i^x S_j^x + S_i^y S_j^y) + J_z S_i^z S_j^z]$$
$$- \mu_B \sum_i (\mathbf{B} \cdot \mathbf{g} \cdot \mathbf{S}), \qquad [1]$$

where the summation runs over the nearest-neighbor $\langle ij \rangle$ sites and the last term is a shorthand notation for the Zeeman term with anisotropic g-factors. The second nearest-neighbor interactions in the ab plane and the near-neighbor interactions between the
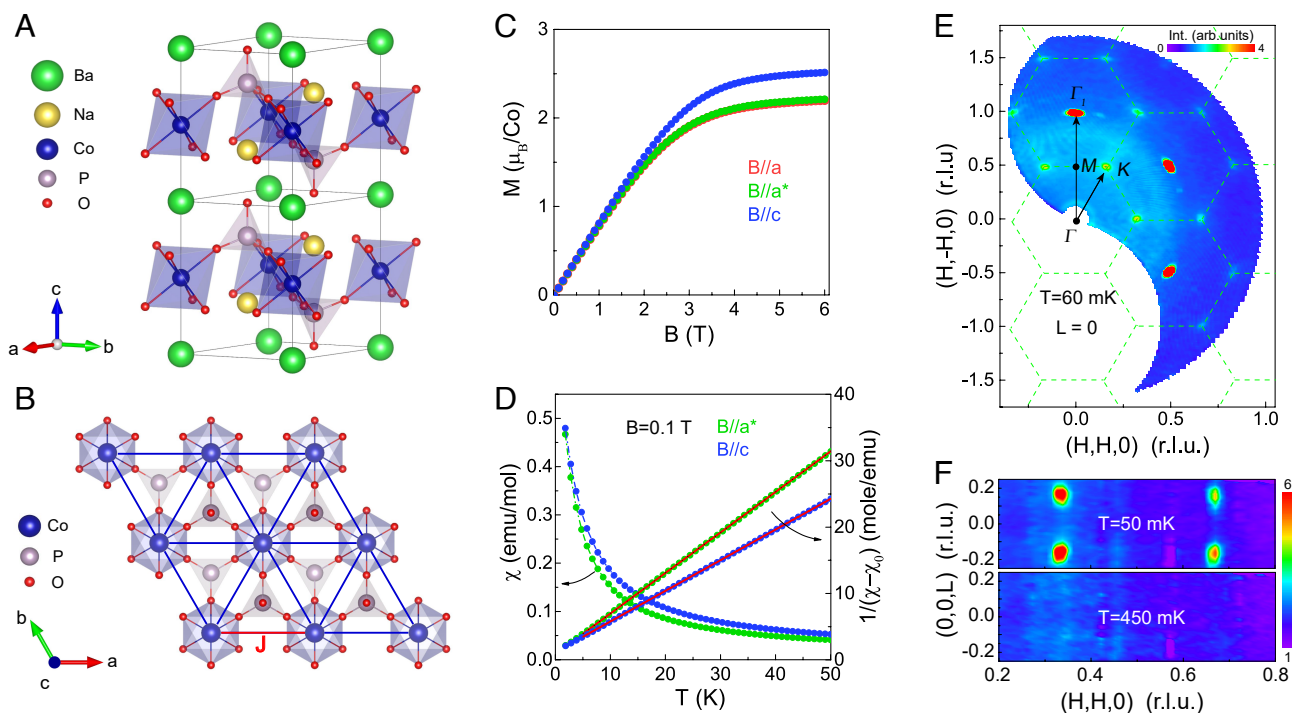

Fig. 1. Crystal structure, magnetization, and neutron diffraction image. (*A*) Crystal structure of $Na_2BaCo(PO_4)_2$. (*B*) Triangular layer of magnetic CoO_6 prism in the ab plane. *J* is the nearest-neighbor exchange interaction. (*C*) Isothermal magnetization, $M(B)$, measured at 2 K with field applied along the a, a^*, c directions. (*D*) Temperature dependence of magnetic susceptibility, χ, and inverse susceptibility, $1/\chi$, in field 0.1 T along the a^*, c directions. Solid lines are the fits using the Curie-Weiss law between 5 K and 50 K. Diffraction image in the (*E*) (H, K, L = 0) scattering plane collected at T= 50 mK and B=0 T with the intensity integrated from [−0.25,0.25] along the vertical [0,0,L] direction and (*F*) (H, H, L) scattering plane measured at T=50 mK < T_N and T = 450 mK > T_N in zero fields, respectively, with the intensity integrated from [−0.05, 0.05] along the vertical [H, −H, 0] direction.

triangular layers along the c direction are neglected here, and the details are explained in part 9 of *SI Appendix*. The local crystal field gives rise to the anisotropic exchange interactions and effective g-factors with the values of $J_{xy} = 1.00(1)$ K, $J_z = 1.73(1)$ K, $g_{ab} = 4.17(1)$ and $g_c = 4.79(1)$ extracted from the Curie–Weiss fitting in Fig. 1D, according to $J_{xy/z} = 3\theta_{CW}^{ab/c}/(zS(S+1))$ and $\mu_{eff}^{ab/c} = g_{ab/c}\mu_B\sqrt{S(S+1)}$ with the number of nearest neighbors $z = 6$ and spin $S = 1/2$. The parameters for the XXZ model Eq. **1** are justified by the magnon dispersion in Fig. 4B as further discussed later.

Neutron Diffraction and Zero-Field Antiferromagnetic Ordering. From the single crystal neutron diffraction experiments in $Na_2BaCo(PO_4)_2$, clear magnetic Bragg peaks were uncovered at K points at 50 mK (Fig. 1 E and F), suggesting the presence of a long-range magnetic order ground state. All observed magnetic reflections can be indexed using magnetic wave vectors $k_m = (1/3, 1/3, k_c = \pm0.167(3))$(Fig. 1$F$). For such magnetic wave vector in $Na_2BaCo(PO_4)_2$, the spin configuration can be described by three different irreducible representations (*SI Appendix*, Table S1). For Γ_1, the spins are parallel to the c axis with a UUD configuration in each layer with k_c modulating the amplitude along the c-axis (*SI Appendix*, Fig. S4A). For Γ_2 and Γ_3, the spin configurations are degenerate 120° spin structure of antiphase chirality, and the spins rotate along the c-axis with an angle $k_c \cdot r$ (*SI Appendix*, Fig. S4 B and C). A combined representation of Γ_1 and Γ_2 was also considered. The spin configuration is a combination of the magnetic structure Γ_1 and Γ_2, with partial spin component forming a 120° structure in the ab-plane and a UUD configuration along the c-axis (*SI Appendix*, Fig. S4D). In addition, it is worthy to note that if we combined Γ_1, Γ_2, and Γ_3 and fixed the ratio of $\Gamma_2/\Gamma_3 = 1 : -1$, a "Y"-shaped spin configuration could be obtained (*SI Appendix*, Fig. S4E), which corresponds to the ground state of the easy-axis XXZ model for $S = 1/2$ TAF (16). However, the fitting results for all the abovementioned models are comparable to each other, due to the limited magnetic reflections, and it is hard to uniquely determine the spin configuration of the ground state. Detailed discussions of the magnetic structure refinements are presented in part 3 of *SI Appendix*. Besides these, all these refinements lead to a greatly reduced ordered moment around 0.54(2) μ_B/Co, which is much smaller than the fully saturated moment, indicating the presence of strong quantum fluctuations in the ordered state.

Quantum Phases Controlled by Magnetic Fields. Fig. 2 A and B are the field-dependent magnetization, M, normalized by the saturation moment M_s (red empty circles), at 60 mK for both field directions. Unlike in the higher-temperature data shown in Fig. 1C, plateau-like features start to build up at low temperatures. This is more clearly seen in the magnetic field derivative of magnetization, dM/dB, shown by green lines in Fig. 2 A and B.

For $B \parallel a^*$, a small cusp is observed in the field-dependent M/M_s curve, and the magnetic susceptibility, dM/dB, exhibits a broad peak around 0.51 T, indicating an additional field-induced phase at base temperature. With further increasing field, a sharp peak at 1.55 T is observed, above which the system is tuned into a fully polarized state. Although the magnetization at the first critical field, 0.51 T, is close to $M/M_s = 1/3$, no complete plateau in the magnetization has been established at this temperature for $B \parallel a^*$.

The situation is quite different for $B \parallel c$. As seen in Fig. 2B, the M/M_s curve exhibits a clear plateau at $M/M_s = 1/3$ between 0.5 and 1.05 T, consistent with the integrated AC susceptibility reported earlier (36). The field range of the 1/3 magnetic plateau states is evaluated to be $0.28 < B/B_s < 0.58$, and this is much wider compared to the 1/3 plateau identified in a similar $S = 1/2$ triangular antiferromagnet $Ba_3CoSb_2O_9$ and the theoretical calculations (24, 39, 40). In addition, extra maximum-like anomalies are observed in dM/dB for $B \parallel c$ before the system is fully polarized, indicating additional field-induced phases, illustrated by the different vertical color bars in Fig. 2B.

Additional evidence of successive field-induced phases is provided by the MCE measurements, which are shown for both field directions in Fig. 2 C and D (the complete MCE data set is presented in *SI Appendix*, Fig. S11). In MCE measurement, the sample temperature variation is recorded as a function of changing magnetic field, in a quasi-adiabatic condition (18, 41, 42). The phase boundaries determined from dM/dB and the anomalies in the MCE curves are in good agreement with each other.

The evolution of the anomalies in dM/dB with increasing temperature is presented in Fig. 2 E and F. For $B \parallel c$, the dip-like features disappear as the temperature is raised to about 150 mK. With further increasing temperature, the 1/3 magnetization plateau gradually disappears around 350 mK (Fig. 2F). The contour plots of the magnetic susceptibility, dM/dB, are summarized in Fig. 2 G and H, with the phase boundaries extracted from the peak positions in the field- and temperature-dependent magnetization measurements (*SI Appendix*, Figs. S5–S7). It is interesting to notice that these peak-like anomalies in dM/dB around the saturation field shown in Fig. 2 B and F are rather broad for all the temperatures accessed. This is due to the presence of the strong quantum fluctuations in this quantum critical region. These peaks are more like crossovers rather than sharp phase transitions at these finite temperatures, and these center positions extend linearly to the critical saturation field at zero temperature (red empty stars in Fig. 2H).

To further characterize the field-induced quantum phase transitions in $Na_2BaCo(PO_4)_2$, specific heat measurements were performed. Fig. 3A shows the zero-field specific heat, C_p, down to 70 mK. The specific heat of the nonmagnetic isostructural compound, $Na_2BaMg(PO_4)_2$, was measured in the same temperature range (green line in Fig. 3A) and used for the estimation of the phonon contribution. The magnetic specific heat, C_M, with phonon contribution subtracted is presented in Fig. 3B. We observe a broad, hump-like anomaly, which extends over a wide temperature range centered around about 1 K, suggesting the establishment of a short-range order hosting a great amount of spin fluctuations. With further decreasing temperature, the fluctuating spins are gradually frozen, and a long-range AFM order is established at $T_N = 150$ mK, as revealed by a sharp λ-type peak in specific heat. A peak in the temperature derivative of magnetization, dM/dT, is also observed at about 150 mK (*SI Appendix*, Fig. S5), consistent with the specific heat measurements. The magnetic entropy calculated from the measured specific heat is shown by the red line in Fig. 3B. In order to obtain the full entropy of $R\ln2$ of the effective spin-1/2 doublet ground state, a residual entropy of about 0.1 $R\ln2$ was added to account for the inaccessible temperature region below 70 mK. Nevertheless, even with this residual contribution included, the magnetic entropy released at the phase transition temperature is relatively small, only about 0.25 $R\ln2$ at $T_N = 0.15$ K, indicating that a great amount
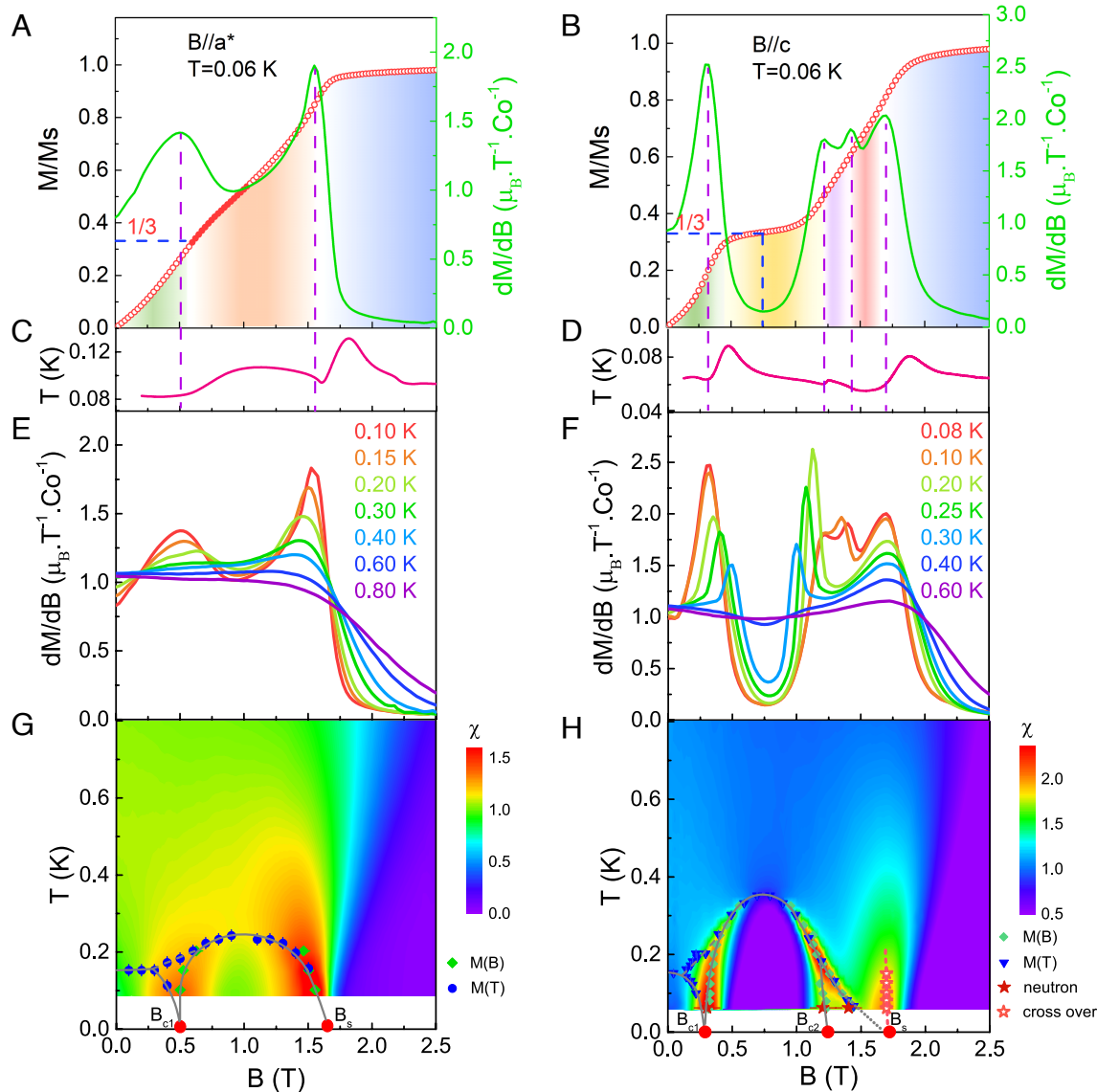
Fig. 2. Magnetization, magnetocaloric effect (MCE), and magnetic phase diagram of Na$_2$BaCo(PO$_4$)$_2$ at ultralow temperatures. (*A* and *B*) Field-dependent normalized magnetization, M/M_S, (red circles) and magnetic susceptibility, dM/dB, (green lines) of Na$_2$BaCo(PO$_4$)$_2$ measured at 60 mK with applied field along the a^* and c directions, respectively. (*C* and *D*) Magnetocaloric effect measured at constant system temperature at about 80 mK and 60 mK by sweeping magnetic field up with applied field along the a^* and c directions, respectively. (*E* and *F*) Field-dependent differential magnetic susceptibility, dM/dB, measured at different temperatures with applied field along the a^* and c directions, respectively. (*G* and *H*) The field-temperature magnetic phase diagram overlaid on the contour plots of magnetic susceptibility dM/dB with field along the a^* and c directions. The magnetic phase boundaries are extracted through the magnetization and neutron diffraction measurements as indicated.

of moment fluctuations are present not only above the phase transition but also persist deep inside the ordered state. This is consistent with our neutron-scattering results with a greatly reduced ordered moment and is also the most recently reported μSR result (43). More details of the entropy in field-induced phases are shown in *SI Appendix*, Figs. S9 and S10.

The temperature-dependent specific heat measured at different magnetic fields is shown in Fig. 3 *C* and *D*, and more detailed data are shown in *SI Appendix*, Figs. S9 and S10. The field-induced magnetic order is revealed by peaks in specific heat. With increasing the magnetic field, the phase transition firstly shifts toward higher temperature and then back to lower temperature, after reaching the maximum at $T \approx$ 0.24 K and 0.37 K for $B \parallel a^*$ and $B \parallel c$, respectively (Fig. 3 *C* and *D*). The peak positions extracted from the specific heat measurements are plotted in Fig. 3 *E* and *F*; these results are consistent with

the phase boundaries extracted from the magnetic susceptibility (Fig. 2 *G* and *H*).

The local trigonal prism crystalline electrical field (CEF) results in the anisotropic g-factors and Ising-like exchange interaction, $J_z/J_{xy} \simeq 1.73$. Previous theoretical studies (16, 17) on the easy axis XXZ model in Eq. **1** indicate a "Y"-shape spin configuration in the zero-field ground state, which is also included in the candidate magnetic structures as we discussed above. Theoretically, the magnetic field with $B \parallel c$ induces successive magnetic quantum phase transitions at zero temperature with the different spin configurations, i.e., "Y"-shape, uud 1/3-plateau phase, "V"-shape, and fully polarized states. A small in-plane field with $B \parallel ab$ reorients the zero-field c-axis "Y" spin configuration into the in-plane inverted-"Y" one. The increasing field with $B \parallel ab$ induces the spin system into the in-plane "V" shape and further into the fully polarized state. The theoretical phase transitions are
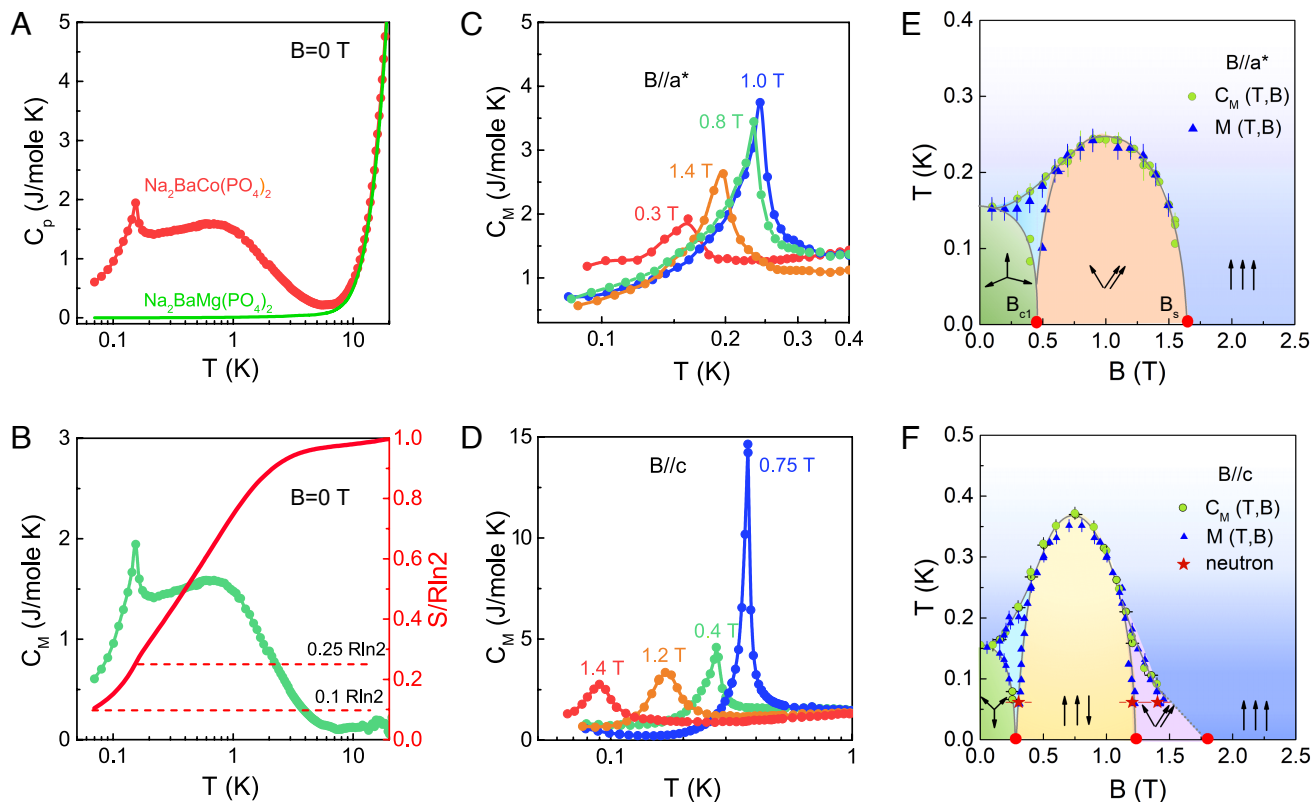
Fig. 3. Specific heat and magnetic phase diagram at low temperatures. (A) Zero-field specific heat, C_p, of $Na_2BaCo(PO_4)_2$ (red circles) and $Na_2BaMg(PO_4)_2$ (green line). (B) Magnetic specific heat, C_M, of $Na_2BaCo(PO_4)_2$ (green circles) at zero field. Magnetic entropy (red line), where the integration range is from 0.07 to 20 K. (C and D) Low-temperature magnetic specific heat, C_M, for $Na_2BaCo(PO_4)_2$ measured at different fields along the $a*$ and c directions, respectively. (E and F) Field-temperature magnetic phase diagram with field along the $a*$ and c directions, respectively. The magnetic phase boundaries are extracted from $M(T,B)$, $C(T,B)$ and neutron diffraction measurements.

consistent with the experimental phase diagrams in Fig. 3 *E* and *F*, and we then mark the theoretical spin configurations accordingly, although these magnetic structures need further confirmations in the future neutron-scattering experiments.

Neutron Scattering and Spin Wave Dispersion. Neutron scattering experiments in the $[HK0]$ scattering plane with magnetic field along the c-axis were also performed. Fig. 4*A* is the field evolution of magnetic order of $Na_2BaCo(PO_4)_2$ measured at 60 mK. The AFM wave vectors are always located at K points in the $(HK0)$ plane, while the locations modulate along the $(00L)$ direction with increasing field along the c-axis. At the first critical field at 0.3 T, where the system was tuned into the 1/3 plateau phase, the zero-field magnetic wave vector only slightly shifts, and an enhancement of the peak intensity was observed. At the second critical field at 1.2 T, in contrast to the weak anomaly observed in the field derivative magnetic susceptibility dM/dB (Fig. 2*B*), an abrupt jump of the wave vector was observed, where the new magnetic wave vector was found to be $[1/3, 1/3, 0.307(6)]$. With further increasing field, these magnetic peaks disappeared around 1.4 T, which is consistent with the phase diagram extracted from the magnetic susceptibility and specific heat measurements (Figs. 2*H* and 3*F*). We have to mention that, at $T = 60$ mK, no well-established magnetic peaks were resolved in between 1.4 T and the saturation field B_s. This suggests that the static ordering temperature of this field region is likely to be below the measuring temperature.

The relative small critical field of $Na_2BaCo(PO_4)_2$ provides us a rare opportunity to justify the spin-1/2 XXZ Hamiltonian Eq. **1** derived from our magnetization measurements. The large

field polarizes the system into a fully polarized ferromagnetic state, and the classical linear spin wave theory turns out to be exact for the single-spin-flip, i.e., magnon excitation. Shown in Fig. 4*B* is the spin wave dispersion of $Na_2BaCo(PO_4)_2$ measured along $M - K - \Gamma_1 - M$ directions in the fully polarized state with an applied magnetic field $B = 3.5$ T. We found that an energy gap around 0.484 (5) meV arose at the K point. The energy dispersion shown by the black empty circles in Fig. 4*B* was extracted from the fitted center positions of Gaussian functions. Spin wave excitations were simulated using the spin-1/2 XXZ Hamiltonian Eq. **1** with the nearest neighbor exchange interactions $J_{xy} = 0.882(7)$ K, and $J_z = 1.451(9)$ K (blue solid line in Fig. 4*B*), which match well with the data in the whole Brillouin zone region. Detailed discussion of the linear spin-wave fitting could be found in part 9 of *SI Appendix*. These exchange parameters extracted through neutron scattering here are also consistent with those values determined from the Curie–Weiss fitting based on the magnetization data (Fig. 1*D*). The energy dispersions along the $(00L)$ direction were presented in Fig. 4*C*. In contrast to the remarkable momentum dependence in the $(HK0)$ triangular plane, flat modes were observed at all high symmetry points (Γ_1, M, and K) along the $(00L)$ direction, suggesting a negligible dispersion along the c-axis. Therefore, we can map the system onto a two-dimensional dilute bose gas of the magnon excitation, which possesses a two-dimensional QCP with the Bose–Einstein condensation of diluted free bosons (magnons).

Field-Induced Quantum Criticality. The overview of the field-dependent magnetic specific heat measurement is presented in
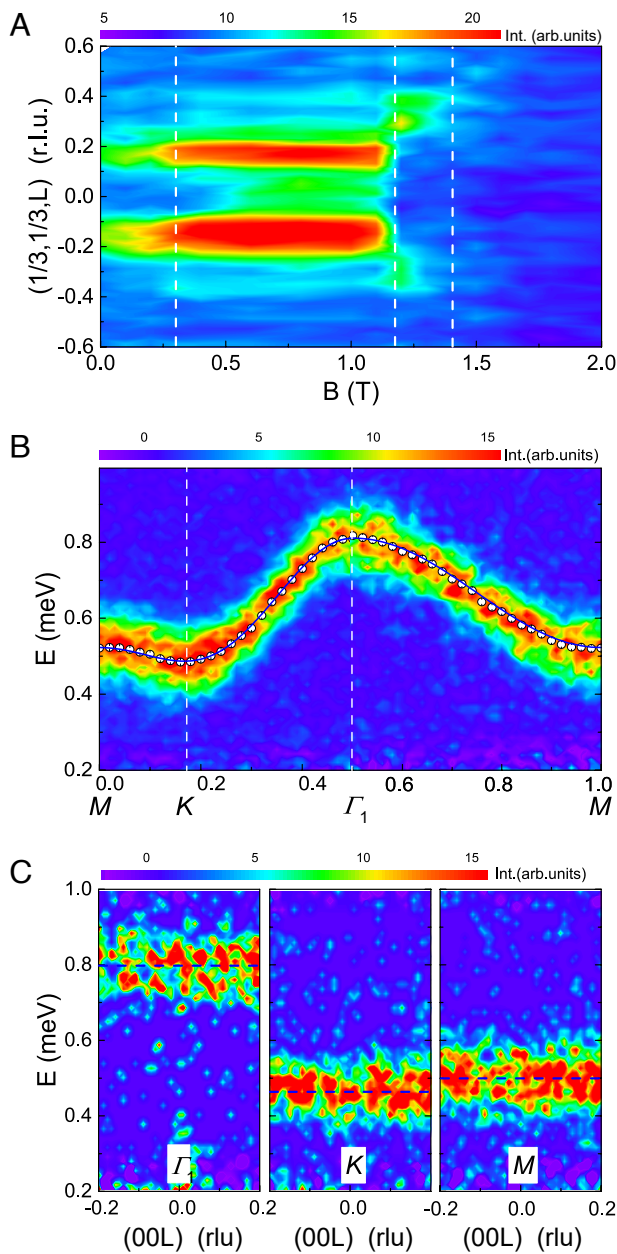
Fig. 4. Neutron-scattering results of $Na_2BaCo(PO_4)_2$. (*A*) Field-dependent magnetic order parameter measured at $T = 60$ mK with $B \parallel c$. The elastic signal was integrated over energy $\Delta E = [-1, 1]$ meV with incident energy $E_i = 23.64$ meV at K point. The field-induced critical fields are marked as vertical dashed lines. (*B*) Contour maps of the experimental spin wave dispersion along $M - K - \Gamma_1 - M$ direction in the fully polarized state, in field $B = 3.5$ T and at temperature $T = 50$ mK. The empty circles with error bars are the fitted center positions, and the solid blue curve is the simulated linear spin wave dispersion, using the spin exchange interactions described in the main text. (*C*) Flat spin wave dispersion along (00L) direction at different high symmetry points (Γ, M and K), measured in the fully polarized state of $Na_2BaCo(PO_4)_2$ with $B = 3.5$ T and at temperature $T = 50$ mK. The blue dashed lines are guides of eyes.

Fig. 5 *A* and *B*, and contour maps of the measured specific heat are presented in Fig. 5 *C* and *D*. The crossover behaviors extracted from the broad maximum of the field-dependent C_p/T were marked by the blue stars for both field directions. In the contour maps, the blue stars extend nearly linearly to zero temperature for both field directions (blue dashed lines in Fig. 5 *C* and *D*),

$$T^* \propto (B - B_c)^{\nu z}, \qquad [2]$$

with the dynamical critical exponents $\nu z_{ab} = 0.93(24)$ and $\nu z_c = 0.93(12)$ obtained by fitting the crossover behaviors for both field directions. This provides a strong constraint on the universality class of the field-induced QCP at the saturation field in $Na_2BaCo(PO_4)_2$.

In addition to the specific heat, an independent check of the universality class is provided by magnetic susceptibility scaling. Assuming the validity of hyperscaling, the scaling function of the magnetic susceptibility can be derived from the field derivative of the free energy (30, 31, 33, 49, 50),

$$\frac{dM}{dB} \cdot T^{\beta} = f\left(T/(B - B_s)^{\nu z}\right), \qquad [3]$$

where $\beta = 2/\nu z - (d + z)/z$. Upon properly adjusting the values of the critical exponents, all the measured susceptibility curves collapse onto a single universal curve, as shown in Fig. 5 *E* and *F*. (More details are given in part 8 of *SI Appendix*.) From this scaling analysis, we obtain $\nu z = 1$ for fields along both directions and $\beta = 0.1$ and $\beta = 0.23$ for $B \parallel a^*$ and $B \parallel c$, respectively. For a two-dimensional BEC universality class with $d = 2$, $z = 2$, and $\nu = 1/2$, the ideal scaling hypothesis would lead to $\beta = 0$. Although there is a slight deviation of the experimentally obtained β from the expected value of exact zero, the observation of the universal quantum critical scaling for both field directions in $Na_2BaCo(PO_4)_2$ is truly remarkable and has not been so clearly identified in 2D frustrated triangular quantum magnets before.

Discussion and Conclusions

The 2D scaling of the thermodynamic properties is noteworthy in $Na_2BaCo(PO_4)_2$. To reconcile the theory and experiment, we examine the interlayer superexchange interaction in $Na_2BaCo(PO_4)_2$. The detailed superexchange paths are shown in *SI Appendix*, Fig. S15. The interlayer coupling contains the c-axis directional nearest-neighbor exchange $J_c \sum_{\langle ij \rangle_c} \mathbf{S}_i \cdot \mathbf{S}_j$ and also next-nearest neighbor ones $J'_c \sum_{[ij]_c} \mathbf{S}_i \cdot \mathbf{S}_j$. The interlayer coupling results in the c-axis Fourier dispersion $\omega_c = 2(J_c + 2J'_c(\cos(\mathbf{k} \cdot \mathbf{a}_1) + \cos(\mathbf{k} \cdot \mathbf{a}_2) + \cos(\mathbf{k} \cdot (\mathbf{a}_1 + \mathbf{a}_2)))) \cos(\mathbf{k} \cdot \mathbf{c})$, where $\mathbf{k}$ is the wave vector, and $\mathbf{a}_{1,2}$ and $\mathbf{c}$ are the in-plane and c directional primitive unit cell vectors, respectively. In $Na_2BaCo(PO_4)_2$, the ordered phase near the saturation field B_s for both $B \parallel c$ and $B \parallel ab$ has the ordering wave vector $\mathbf{k} = (1/3, 1/3, k_c)$, and the c-axis dispersion of the interlayer coupling is $\omega_c = 2(J_c - 3J'_c) \cos(k_c)$. In $Na_2BaCo(PO_4)_2$, the superexchange interactions between the spins on Co^{2+} ions are mediated by PO_4 tetrahedron. Most importantly, for a simple counting, J_c has three exchange paths, while J'_c has one (*SI Appendix*, Fig. S15). If we assume that the c-axis directional interlayer superexchange paths of the nearest-neighbor and next-nearest neighbor interlayer couplings are equivalent, this results in $J_c = 3J'_c$. This then allows a perfect cancellation of the interlayer couplings of $Na_2BaCo(PO_4)_2$ for the single magnon $\omega_c = 0$ near the saturation field. We stress that this cancellation is only an approximation since these two exchange paths cannot be exactly identical. However, the threefold symmetry makes this approximation very promising. We have to mention that this dimensional reduction appears only at the QCP near the saturation fields where the ordering moment vanishes. Away from the saturation field, the ordering moment is finite, and the effect of the interlayer coupling has the high-order effect and results in the competing effective coherent interlayer hopping (8),
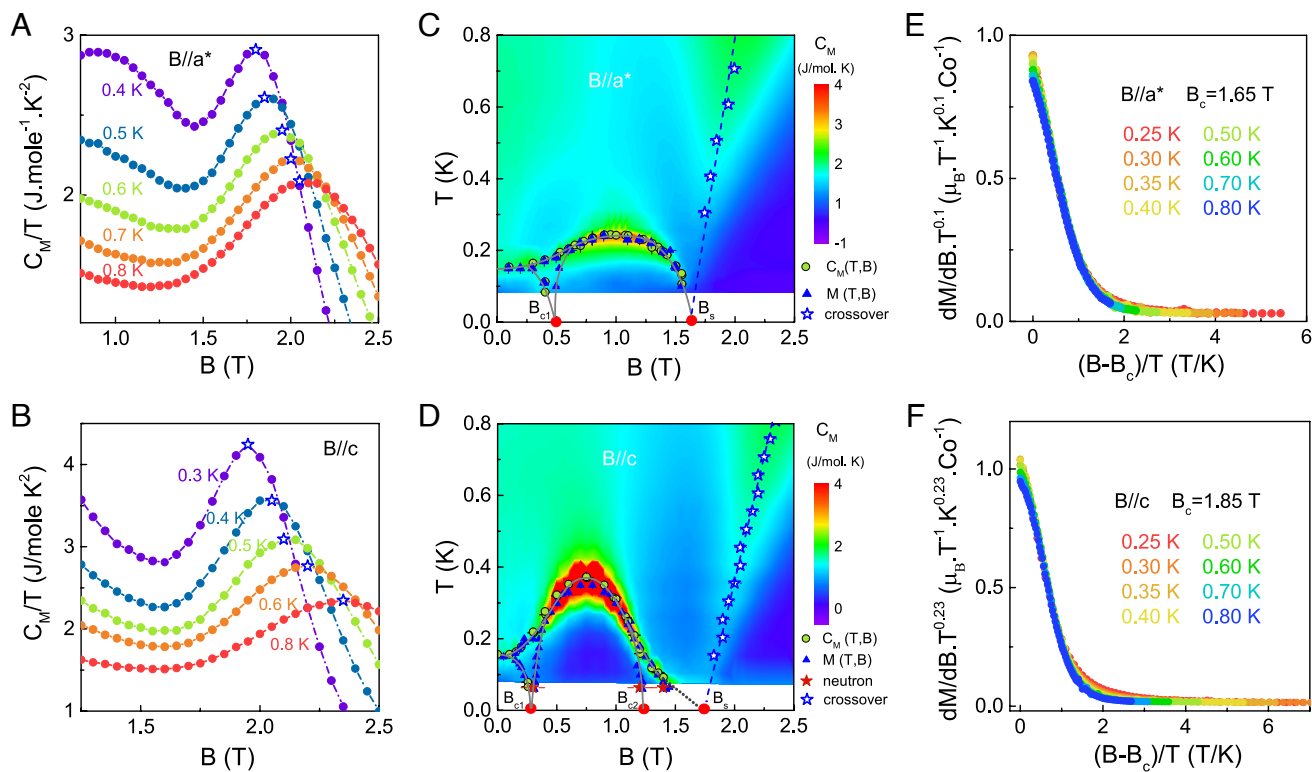
Fig. 5. Quantum criticality of $Na_2BaCo(PO_4)_2$. (*A* and *B*) Field-dependent magnetic specific heat, C_M/T, at different temperatures with field along the $a*$ and c directions, respectively. (*C* and *D*) Contour plots of the magnetic specific heat with the magnetic phase diagram overlaid. The blue dashed lines indicate a crossover associated with the broad maximum observed for both field directions. (*E* and *F*) Critical scaling of the magnetic susceptibility with field along the $a*$, c directions, respectively.

probably accounting for the zero-field incommensurate ordered wave vector at low fields.

The narrow magnon bandwidth rendered by the strong geometrical frustration can give rise to various exotic magnetic quantum states, and the related field-induced quantum criticality constitutes an essential part of condensed matter physics. Although a variety of frustrated systems have been studied, a clear demonstration of a 2D QCP of BEC type with dynamical exponent $z = 2$ in real quantum magnets remains unusual. An important reason is that the weakly three-dimensional couplings always play a role in real materials as the temperature approaches zero. However, the characteristic universal scaling and the linear crossover behaviors of $Na_2BaCo(PO_4)_2$ distinctly demonstrate a field-induced QCP dominated by the 2D quantum fluctuations, and the inelastic neutron-scattering results together with the analysis of the superexchange paths suggest that $Na_2BaCo(PO_4)_2$ may serve as another rare example of emergent dimensional reduction which protects the 2D criticality at $T = 0$. The relatively low critical fields of $Na_2BaCo(PO_4)_2$ is also remarkable, which provide a great opportunity for studying the field-induced quasiparticle crystal phases and universal quantum behaviors through various experimental techniques.

Materials and Methods

Materials Synthesis. $Na_2BaCo(PO_4)_2$ single crystals used in this study were grown by the NaCl-flux method (35). The starting powder materials Na_2CO_3 (alfa, 99.5%, $BaCO_3$ (alfa, 99.95%), CoO (aladdin, 99%), $(NH_4)_2HPO_4$ (aladdin, 99.99%), and NaCl (alfa, 99.99%) were ground thoroughly in a molar ratio of 1:1:1:2:5. Then, the mixture was loaded in an alumina crucible with a lid

and heated up to 850°C for 20 h followed by a slow cooling procedure to 750°C in 100 h. After soaking in water to remove the residual NaCl, plenty of hexagonal pink single crystals were mechanically separated from the crucible wall.

Magnetization and Thermodynamic Measurements. For magnetization measurements, two different magnetometers were used for different temperature ranges: i) commercial Magnetic Property Measurement System (MPMS-Quantum Design) with DC measurement mode for temperature range $T = 1.8$–300 K and ii) a high-sensitive Hall sensor magnetometer (51–53) with dilution refrigerator insert for the lower-temperature range $T = 0.05$–2 K. For the specific heat measurements, a traditional relaxation time method was used, with a dilution refrigerator insert down to 50 mk in the Quantum Design Physical Property Measurements System (PPMS). For the MCE measurements, a pre-calibrated Lakeshore Cernox semiconductor sensor was used, and the field sweeping rate was set at 20 Oe/s (54).

Neutron Scattering Measurements. The neutron-scattering experiments were performed using the time-of-flight cold neutron spectrometer, PELICAN, with fixed incident energy E_i=3.71 meV (energy resolution is about 0.15 meV) at the Open Pool Australian Lightwater (OPAL) reactor at Australia's Nuclear Science and Technology Organisation (ANSTO) (55) and the cold-neutron disk chopper spectrometer (AMATERAS, BL14 beamline), with fixed incident energy E_i=23.65 meV (energy resolution is about 1.2 meV) in the Facility (MLF) at the Japan Proton Accelerator Research Complex (J-PARC) (56). Hundreds of samples were co-aligned on oxygen-free copper sheets with total mass about 3 g and cooled using a dilution refrigerator insert in a 7-T magnet on both spectrometers. The magnetic field was applied along the c-axis of the sample, and the data were collected at 50 mK, 60 mK, and 450 mK with different magnetic fields. The data were processed using a combination of the freely available Data Analysis and

Visualization Environment (DAVE) software (57, 58). The magnetic structure of the ground state was analyzed by the representation theory (59).

Data, Materials, and Software Availability. All study data are included in the article and/or SI Appendix.

Author affiliations: [a]Department of Physics, Southern University of Science and Technology, Shenzhen 518055, China; [b]Academy for Advanced Interdisciplinary Studies, Southern University of Science and Technology, Shenzhen 518055, China; [c]Institute of High Energy Physics, Chinese Academy of Sciences, Beijing 100049, China; [d]Spallation Neutron Source Science Center (CSNS), Dongguan 523803, China; [e]Shenzhen Institute for Quantum Science and Engineering, Shenzhen 518055, China; [f]Istituto Sintesi Organica e Fotoreattività (ISOF - CNR) Via P. Gobetti, 101-40129 Bologna, Italy; [g]College of Physics Science and Technology, Yangzhou University, Yangzhou 225002, China; [h]School of Physical Science and Technology & Key Laboratory for Magnetism and Magnetic Materials of the Ministry of Education, Lanzhou University, Lanzhou 730000, China; [i]Department of Chemistry, Southern University of Science and Technology, Shenzhen 518055, China; [j]Japan Proton Accelerator Research Complex (J-PARC) Center, Japan Atomic Energy Agency, Tokai, Ibaraki 319-1195, Japan; [k]Australian Nuclear Science and Technology Organisation, Locked bag 2001, Kirrawee DC, NSW 2232, Australia; [l]Istituto Officina dei Materiali (IOM - CNR), Laboratorio di Tecnologie Avanzate, Superfici e Catalisi (TASC), 34149 Trieste, Italy; [m]Condensed Matter Physics and Materials Science Division, Brookhaven National Laboratory, Upton, NY 11973; and [n]Shenzhen Key Laboratory of Advanced Quantum Functional Materials and Devices, Southern University of Science and Technology, Shenzhen 518055, China

Author contributions: J.S., L. Wu, J.-W.M., and Dapeng Yu designed research; W.J., L.H., J.Y., Y.F., and L. Wang provided single crystals used in this study; J.S., H.G., N.Z., S.W., X.T., and L. Wu carried out the low temperature measurements; J.S., L. Wu, P.M., M.K., R.M., and Dehong Yu carried out the neutron scattering experiments; A.C., and G.B. designed and fabricated the hall sensor magnetometer used in this study; J.R., Q.L., J.Z., B.X., J.-W.M., and I.A.Z. developed theoretical explanations; and J.S., J.-W.M., I.A.Z., Dehong Yu, L. Wu wrote the paper.

1. T. Matsubara, H. Matsuda, Lattice model of liquid helium I. *Prog. Theor. Phys.* **16**, 569–582 (1956).
2. E. G. Batiyev, L. S. Braginsky, Antiferromagnet in a strong magnetic-field-analogy with a Bose-gas. *Zh. Eksp. Teor. Fiz.* **87**, 1361–1370 (1984).
3. M. Fisher, P. Weichman, G. Grinstein, D. Fisher, Boson localization and the superfluid-insulator transition. *Phys. Rev. B* **40**, 546 (1989).
4. T. Giamarchi, A. M. Tsvelik, Coupled ladders in a magnetic field. *Phys. Rev. B* **59**, 11398 (1999).
5. M. Greiner, O. Mandel, T. Esslinger, T. W. Hänsch, I. Bloch, Quantum phase transition from a superfluid to a Mott insulator in a gas of ultracold atoms. *Nature* **415**, 39 (2002).
6. T. M. Rice, To condense or not to condense. *Science* **298**, 760 (2002).
7. T. Giamarchi, C. Rüegg, O. Tchernyshyov, Bose-Einstein condensation in magnetic insulators. *Nat. Phys.* **4**, 198 (2008).
8. V. Zapf, M. Jaime, C. D. Batista, Bose-Einstein condensation in quantum magnets. *Rev. Mod. Phys.* **86**, 563 (2014).
9. S. Haravifard et al., Crystallization of spin superlattices with pressure and field in the layered magnet SrCu₂(BO₃)₂. *Nat. Commun.* **7**, 11956 (2016).
10. S. Sachdev, *Quantum Phase Transitions* (Cambridge University Press, ed. 2, 2011).
11. S. Miyashita, Magnetic properties of Ising-like Heisenberg antiferromagnets on the triangular lattice. *J. Phys. Soc. Jpn.* **55**, 3605 (1986).
12. A. V. Chubukov, D. I. Golosov, Quantum theory of an antiferromagnet on a triangular lattice in a magnetic field. *J. Phys. Condens. Matter* **3**, 69 (1991).
13. O. A. Starykh, Unusual ordered phases of highly frustrated magnets: A review. *Rep. Prog. Phys.* **78**, 052502 (2015).
14. A. A. Burkov, L. Balents, Superfluid-insulator transitions on the triangular lattice. *Phys. Rev. B* **72**, 134502 (2005).
15. H. C. Jiang, M. Q. Weng, Z. Y. Weng, D. N. Sheng, L. Balents, Supersolid order of frustrated hard-core bosons in a triangular lattice system. *Phys. Rev. B* **79**, 020409 (2009).
16. D. Yamamoto, G. Marmorini, I. Danshita, Quantum phase diagram of the triangular-lattice XXZ model in a magnetic field. *Phys. Rev. Lett.* **112**, 127203 (2014).
17. D. Yamamoto, G. Marmorini, M. Tabata, K. Sakakura, I. Danshita, Magnetism driven by the interplay of uctuations and frustration in the easy-axis triangular XXZ model with transverse fields. *Phys. Rev. B* **100**, 140410 (2019).
18. T. Ono et al., Magnetization plateau in the frustrated quantum spin system Cs₂CuBr₄. *Phys. Rev. B* **67**, 104431 (2003).
19. T. Ono et al., Magnetization plateaux of the S = 1/2 two-dimensional frustrated antiferromagnet Cs₂CuBr₄. *J. Phys. Condens. Matter* **16**, S773 (2004).
20. H. Tsujii et al., Thermodynamics of the up-up-down phase of the S = 1/2 triangular-lattice antiferromagnet Cs₂CuBr₄. *Phys. Rev. B* **76**, 060406 (2007).
21. N. A. Fortune et al., Cascade of magnetic-field-induced quantum phase transitions in a spin-1/2 triangular-lattice antiferromagnet. *Phys. Rev. Lett.* **102**, 257201 (2009).
22. Y. Shirata, H. Tanaka, A. Matsuo, K. Kindo, Experimental realization of a spin-1/2 triangular-lattice Heisenberg antiferromagnet. *Phys. Rev. Lett.* **108**, 057205 (2012).
23. H. D. Zhou et al., Successive phase transitions and extended spin-excitation continuum in the S = 1/2 triangular-lattice antiferromagnet Ba₃CoSb₂O₉. *Phys. Rev. Lett.* **109**, 267206 (2012).
24. T. Susuki et al., Magnetization process and collective excitations in the S = 1/2 triangular-lattice heisenberg antiferromagnet Ba₃CoSb₂O₉. *Phys. Rev. Lett.* **110**, 267201 (2013).
25. X. Z. Liu et al., Microscopic evidence of a quantum magnetization process in the S = 1/2 triangular-lattice Heisenberg-like antiferromagnet Ba₃CoSb₂O₉. *Phys. Rev. B* **100**, 094436 (2019).
26. M. M. Bordelon et al., Field-tunable quantum disordered ground state in the triangular-lattice antiferromagnet NaYbO₂. *Nat. Phys.* **15**, 1058 (2019).
27. K. M. Ranjith et al., Anisotropic field-induced ordering in the triangular-lattice quantum spin liquid NaYbSe₂. *Phys. Rev. B* **100**, 224417 (2019).
28. J. Xing et al., Field-induced magnetic transition and spin uctuations in the quantum spinliquid candidate CsYbSe₂. *Phys. Rev. B* **100**, 220407 (2019).
29. J. Ma et al., Spin-orbit-coupled triangular-lattice spin liquid in rare-earth chalcogenides. arXiv [Preprint] (2020). http://arxiv.org/abs/2002.09224
30. A. Schröder et al., Onset of antiferromagnetism in heavy-fermion metals. *Nature* **407**, 351 (2000).
31. A. Bianchi, R. Movshovich, I. Vekhter, P. G. Pagliuso, J. L. Sarrao, Avoided antiferromagnetic order and quantum critical point in CeCoIn₅. *Phys. Rev. Lett.* **91**, 257001 (2003).
32. B. Yang et al., Quantum criticality and the Tomonaga-Luttinger liquid in one-dimensional Bose gases. *Phys. Rev. Lett.* **119**, 165701 (2017).
33. L. S. Wu et al., Tomonaga-Luttinger liquid behavior and spinon confinement in YbAlO₃. *Nat. Commun.* **10**, 698 (2019).
34. A. M. Tsvelik, *Quantum Field Theory in Condensed Matter Physics* (Cambridge University Press, 2007).
35. R. Zhong, S. Guo, G. Xu, Z. Xu, R. J. Cava, Strong quantum fuctuations in a quantum spin liquid candidate with a Co-based triangular lattice. *Proc. Nat. Acad. Sci.* **116**, 14505 (2019).
36. N. Li et al., Possible itinerant excitations and quantum spin state transitions in the effective spin-1/2 triangular-lattice antiferromagnet Na₂BaCo(PO₄)₂. *Nat. Commun.* **11**, 4216 (2020).
37. D. Yamamoto, G. Marmorini, I. Danshita, Microscopic model calculations for the magnetization process of layered triangular-lattice quantum antiferromagnets. *Phys. Rev. Lett.* **114**, 027201 (2015).
38. A. Abragam, B. Bleaney, *Electron Paramagnetic Resonance of Transition Ions* (OUP Oxford, 2012).
39. D. J. J. Farnell, R. Zinke, J. Schulenburg, J. Richter, High-order coupled cluster method study of frustrated and unfrustrated quantum magnets in external magnetic fields. *J. Phys. Condens. Matter* **21**, 406002 (2009).
40. T. Sakai, H. Nakano, Critical magnetization behavior of the triangular and kagome lattice quantum antiferromagnets. *Phys. Rev. B* **83**, 100405 (2011).
41. V. S. Zapf et al., Bose-Einstein condensation of S=1 nickel spin degrees of freedom in NiCl₂·SC(NH₂)₂. *Phys. Rev. Lett.* **96**, 077204 (2006).
42. Y. Kohama, C. Marcenat, T. Klein, M. Jaime, AC measurement of heat capacity and magnetocaloric effect for pulsed magnetic fields. *Rev. Sci. Instrum.* **81**, 104902 (2010).
43. S. Lee et al., Temporal and field evolution of spin excitations in the disorder-free triangular antiferromagnet Na₂BaCo(PO₄)₂. *Phys. Rev. B* **103**, 024413 (2021).
44. T. Tay, O. I. Motrunich, Variational studies of triangular Heisenberg antiferromagnet in magnetic field. *Phys. Rev. B* **81**, 165116 (2010).
45. O. A. Starykh, H. Katsura, L. Balents, Extreme sensitivity of a frustrated quantum magnet: Cs₂CuCl₄. *Phys. Rev. B* **82**, 014421 (2010).
46. M. Ye, A. V. Chubukov, Half-magnetization plateau in a Heisenberg antiferromagnet on a triangular lattice. *Phys. Rev. B* **96**, 140406 (2017).
47. D. Yamamoto, G. Marmorini, I. Danshita, Magnetization process of spin-1/2 Heisenberg antiferromagnets on a layered triangular lattice. *J. Phys. Soc. Jpn.* **85**, 024706 (2016).
48. M. Li, M. L. Plumer, G. Quirion, Effects of interlayer and bi-quadratic exchange coupling on layered triangular lattice antiferromagnets. *J. Phys. Condens. Matter* **32**, 135803 (2020).
49. Y. Matsumoto et al., Quantum criticality without tuning in the mixed valence compound β-YbAlB₄. *Science* **331**, 316 (2011).
50. L. S. Wu, M. S. Kim, K. Park, A. M. Tsvelik, M. C. Aronson, Quantum critical fluctuations in layered YFe₂Al₁₀. *Proc. Natl. Acad. Sci. U.S.A* **111**, 14088 (2014).

51. Magnetometry by means of Hall micro-probes in the Quantum Design PPMS, *Quantum Design Application Note* 1084-701.

52. A. Cavallini, B. Fraboni, F. Capotondi, L. Sorba, G. Biasiol, Deep levels in MBE grown AlGaAs/GaAs heterostructures. *Microelectron. Eng.* **73**, 954–959 (2004).

53. A. Candini *et al.*, Hall nano-probes fabricated by focused ion beam. *Nanotechnology* **17**, 2105 (2006).

54. S. S. Courts, P. R. Swinehart, Review of cernox^{TM} (zirconium oxy-nitride) thin-film resistance temperature sensors. *AIP Conf. Proc.* **684**, 393–398 (2003).

55. D. H. Yu, R. Mole, T. Noakes, S. Kennedy, R. Robinson, Pelican a time of flight cold neutron polarization analysis spectrometer at OPAL. *J. Phys. Soc. Jpn.* **82**, SA027 (2013).

56. K. Nakajima *et al.*, AMATERAS: A cold-neutron disk chopper spectrometer. *J. Phys. Soc. Jpn.* **80**, SB028 (2011).

57. R. T. Azuah *et al.*, DAVE: A comprehensive software suite for the reduction, visualization, and analysis of low energy neutron spectroscopic data. *J. Res. Natl. Inst. Stan. Technol.* **114**, 341 (2009).

58. R. A. Ewings *et al.*, Horace: Software for the analysis of data from single crystal spectroscopy experiments at time-of-flight neutron instruments. *Nucl. Instrum. Methods Phys. Res. Sect. A* **834**, 132 (2016).

59. J. Rodríguez-Carvajal, Recent advances in magnetic structure determination by neutron powder diffraction. *Phys. B* **192**, 55 (1993).